

# Structural heterogeneity-induced enhancement of transverse magneto-thermoelectric conversion revealed by thermoelectric imaging in functionally graded materials

Sang J. Park, Ravi Gautam, Takashi Yagi, Rajkumar Modak, Hossein Sepehri-Amin & Ken-ichi Uchida

To cite this article: Sang J. Park, Ravi Gautam, Takashi Yagi, Rajkumar Modak, Hossein Sepehri-Amin & Ken-ichi Uchida (2026) Structural heterogeneity-induced enhancement of transverse magneto-thermoelectric conversion revealed by thermoelectric imaging in functionally graded materials, Science and Technology of Advanced Materials, 27:1, 2643965, DOI: [10.1080/14686996.2026.2643965](https://doi.org/10.1080/14686996.2026.2643965)

To link to this article: <https://doi.org/10.1080/14686996.2026.2643965>



© 2026 The Author(s). Published by National Institute for Materials Science in partnership with Taylor & Francis Group.



[View supplementary material](#)



Published online: 31 Mar 2026.



[Submit your article to this journal](#)



Article views: 172



[View related articles](#)



[View Crossmark data](#)

# Structural heterogeneity-induced enhancement of transverse magneto-thermoelectric conversion revealed by thermoelectric imaging in functionally graded materials

Sang J. Park<sup>a</sup>, Ravi Gautam<sup>a</sup>, Takashi Yagi<sup>b</sup>, Rajkumar Modak<sup>c</sup>, Hossein Sepehri-Amin<sup>a</sup> and Ken-ichi Uchida<sup>a,c</sup>

<sup>a</sup>Research Center for Magnetic and Spintronic Materials, National Institute for Materials Science, Tsukuba, Japan;

<sup>b</sup>National Metrology Institute of Japan, National Institute of Advanced Industrial Science and Technology, Tsukuba, Japan;

<sup>c</sup>Department of Advanced Materials Science, Graduate School of Frontier Sciences, The University of Tokyo, Kashiwa, Japan

## ABSTRACT

Functionally graded materials (FGMs) exhibit continuous property variations that enable unique functionalities and provide efficient platforms for systematic property optimization. Here, we report the fabrication of FGMs with graded structural heterogeneity by annealing an amorphous metal under a one-dimensional temperature gradient. Using lock-in thermography (LIT), we spatially mapped transverse thermoelectric conversion with high spatial and temperature resolution. A pronounced non-monotonic response was observed, with the maximum anomalous Ettingshausen effect, a transverse charge-to-heat conversion in magnetic materials, appearing in the atomic-heterogeneity regime well before crystallization. This enhancement was not captured by conventional structural or longitudinal transport measurements, highlighting the exceptional sensitivity of transverse thermoelectric phenomena to subtle structural variations. Structural analyses using scanning transmission electron microscopy and atom probe tomography revealed Fe-based crystalline alloys and Cu nanoclusters embedded in the amorphous matrix, whose heterogeneity accounts for the enhanced response. These findings establish temperature-gradient-annealed FGMs, combined with LIT, as a powerful methodology for probing structural-heterogeneity-driven transverse electron transport and for designing high-performance flexible materials.

## ARTICLE HISTORY

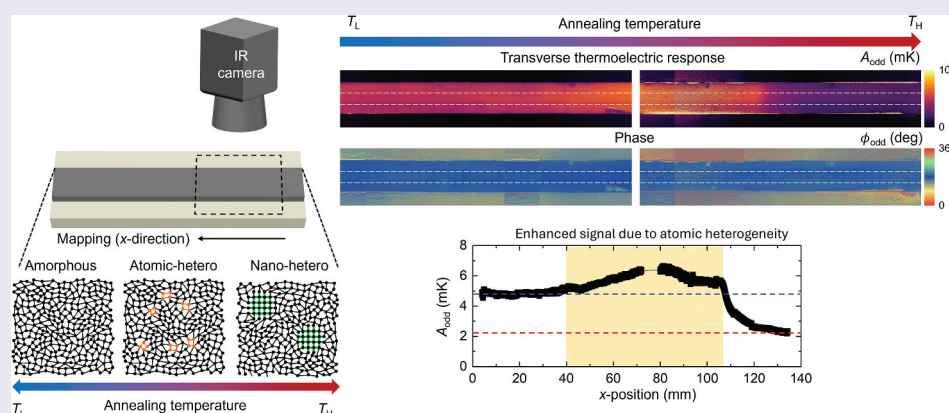
Received 22 December 2025

Revised 9 February 2026

Accepted 8 March 2026

## KEYWORDS

Functionally graded materials; anomalous Ettingshausen effect; lock-in thermography; structural heterogeneity; transverse thermoelectric conversion



## IMPACT STATEMENT


We demonstrate that disorder-graded functionally graded materials combined with thermoelectric imaging directly reveal a non-monotonic enhancement of the anomalous Ettingshausen effect driven by controlled structural heterogeneity.

## 1. Introduction

Functionally graded materials (FGMs) are a class of advanced materials characterized by continuous gradients in composition, microstructure, or porosity

along spatial directions [1–5]. Such continuous variations in material properties impart unique functionalities, such as enhanced mechanical performance [5,6]

**CONTACT** Sang J. Park  PARK.SangJun@nims.go.jp; Ken-ichi Uchida  UCHIDA.Kenichi@nims.go.jp  Research Center for Magnetic and Spintronic Materials, National Institute for Materials Science, 1-2-1 Sengen, Tsukuba, Ibaraki 305-0047, Japan

 Supplemental data for this article can be accessed online at <https://doi.org/10.1080/14686996.2026.2643965>

© 2026 The Author(s). Published by National Institute for Materials Science in partnership with Taylor & Francis Group.

This is an Open Access article distributed under the terms of the Creative Commons Attribution License (<http://creativecommons.org/licenses/by/4.0/>), which permits unrestricted use, distribution, and reproduction in any medium, provided the original work is properly cited. The terms on which this article has been published allow the posting of the Accepted Manuscript in a repository by the author(s) or with their consent.

and efficient energy conversion within solids [7–9], by spatially optimizing material properties. FGMs have been widely adopted across diverse fields, including high-performance composites for aerospace, marine, and nuclear applications [1,10], and energy materials for efficient thermoelectric conversion [7–9]. They offer potential solutions to the limitations of conventional homogeneous materials and heterostructures by overcoming intrinsic property constraints.

Moreover, FGMs provide a unique experimental platform for investigating material properties, owing to their continuous property gradients. If these gradients can be spatially resolved with sufficient precision, efficient parameter studies can be performed by treating the property variations as experimental variables within a single sample. This approach enables characterization and optimization with significantly improved cost-effectiveness and throughput compared to conventional strategies, which typically rely on discrete sample sets and limited parameter sweeps [11–15], thereby often underestimating the maximum potential of materials.

A promising technique for characterizing such continuously varying properties is contactless transport measurement using lock-in thermography (LIT). LIT captures the thermal response of a solid to periodic excitation, offering high temperature sensitivity ( $<1$  mK) [16] and effective separation of the periodic thermal signals from background temperature fluctuations [17], compared to conventional steady-state infrared (IR) measurements [18–20]. These capabilities enable site-specific detection of microscale defects and dislocations in materials such as graphene [17], as well as intrinsic thermoelectric properties such as Seebeck and Peltier coefficients [21,22]. Recently, LIT has also been used to study transverse thermoelectric effects [23–28], such as the anomalous Ettingshausen effects (AEE), which represents the transverse generation of a temperature gradient in magnetic materials in response to an applied longitudinal charge current [29–31].

There have been studies aimed at optimizing the transverse thermoelectric properties by integrating the FGMs with LIT. For instance, Modak et al. [25] fabricated a Heusler  $\text{Co}_2\text{MnAl}_{1-d}\text{Si}_d$  combinatorial film, where the relative compositions of Al ( $1-d$ ) and Si ( $d$ ) were gradually varied along one direction. This FGM film provided a novel platform to investigate the role of chemical composition and Fermi level control in AEE. Using LIT measurements, the optimal AEE performance was revealed specifically in the range  $0.06 < d < 0.12$ , which was higher than that of constituent homogeneous  $\text{Co}_2\text{MnAl}$  ( $d = 0$ ) and  $\text{Co}_2\text{MnSi}$  ( $d = 1$ ) films. Similar approaches have been successfully applied to the development of high-performance spin Hall materials using  $\text{Cu}_d\text{Ir}_{100-d}$  [32] and  $\text{Pt}_d\text{W}_{100-d}$  [24] alloy thin films as well as

magnetic  $\text{Sm}_d\text{Co}_{100-d}$  and  $\text{Sm}_{20}(\text{Co}_{100-d}\text{Fe}_d)_{80}$  thin films [33], all of which benefited from the integration of FGMs and LIT. The key ideas of these demonstrations are (1) the precise control of transverse deflection mechanisms of electrons in solids [34–39] as experimental variables, such as Berry-curvature-driven intrinsic mechanisms and/or extrinsic mechanisms (e.g. skew scattering and side jump mechanisms) within a single FGM sample, and (2) the high-resolution spatial detection of their effects on transverse thermoelectric conversion by measuring the AEE with spatial resolution, enabled by LIT.

Recently, large transverse thermoelectric conversion has been observed in structurally heterogeneous magnetic composites [40–45], with magnitudes comparable to those in single-crystalline topological materials or in epitaxial thin films grown on rigid platforms [30,31,46–53]. Interestingly, such large conversion was demonstrated while retaining mechanical flexibility, suggesting potential applications based on the anomalous Nernst effect (ANE), which is the reciprocal of the AEE and corresponds to transverse heat-to-charge current conversion in magnetic materials. Applications include thermal energy harvesting [40–43,54] and heat flux sensing [44,55–58] from various curved heat sources, such as heat pipes. A recent study combining theoretical model and experimental validation suggested that the large transverse thermoelectric conversion originates from the formation of heterogeneous multi-phase structures [41], which cannot be explained by the above-mentioned conventional theoretical intrinsic and extrinsic frameworks [34–39]. Independent experimental studies have also shown that the heterogeneous formation of nanoclusters and/or local structural disorder in an amorphous matrix effectively increases the transverse thermoelectric conversion [40,42,43]. All these results collectively suggest the important role of structural engineering in transverse thermoelectric conversion, while the detailed mechanisms based on a specific formulation are yet to be fully understood in the complex system.

If the structural characteristic can be spatially controlled within a single sample by fabricating an FGM and the corresponding variation in transverse thermoelectric response is mapped using LIT, the effects of structural heterogeneity on AEE and ANE can be investigated systematically in a statistically significant and high-throughput manner. In addition, such FGMs serve as an ideal platform for determining the optimal degree of heterogeneity that maximizes AEE and ANE, thereby providing high-resolution insight into the relationship between structural heterogeneity and transverse electron transport mechanisms.

Here, we report the observation of transverse thermoelectric conversion in structural-heterogeneity-graded FGM ribbons by measuring the spatial distribution of AEE using LIT. First, we introduce a simple

and scalable fabrication method for bulk FGM ribbons by annealing an Fe-based fully amorphous ribbon under a temperature gradient (Figure 1), where annealing-temperature-driven structural heterogeneity can tune the transverse thermoelectric property [40–43]. We then demonstrate a continuous variation of the AEE response with annealing temperature in the single sample, exhibiting a non-monotonic trend in which the AEE reaches a maximum at a mid-annealing temperature well before crystallization.

Through structural analyses using atom probe tomography (APT) and scanning transmission electron microscopy (STEM), we clarified that the enhanced AEE is strongly correlated with the presence of Fe-based crystalline alloys and/or Cu nanoclusters embedded in the amorphous matrix, providing compelling evidence for the critical role of structural heterogeneity in enhancing transverse electron scattering. This correlation offers design guidelines for transverse thermoelectric materials based on magnetic amorphous alloys. Notably, such subtle structural variations responsible for the AEE enhancement are not captured by conventional characterization techniques such as lab-scale X-ray diffraction (XRD) or longitudinal electrical and thermal transport property measurements, highlighting the unique sensitivity of transverse thermoelectric phenomena to atomic and nanoscale structural heterogeneity.

## 2. Results and discussion

### 2.1. Fabrication of heterogeneity-graded FGM

We first outline the design strategy for fabricating bulk heterogeneity-graded FGMs using amorphous ribbons. An Fe-based amorphous alloy with the composition  $\text{Fe}_{79}\text{Si}_4\text{B}_{14}\text{Nb}_2\text{Cu}_1$  was selected as the demonstration material, as it has been reported to exhibit large AEE under controlled annealing temperatures ( $T_a$ ) while maintaining mechanical flexibility [40,42]. Specifically, the AEE peaks when the sample is annealed in the  $T_a$  range of 523–673 K, and decreases significantly at higher  $T_a$ , indicating the importance of annealing-induced structural heterogeneity, including crystallinity, precipitation, and atomic-scale disorder, for optimizing AEE [42]. The broad  $T_a$  window associated with enhanced AEE performance (523–673 K) also allows for a clear investigation of the relationship between structural change and AEE, making this alloy system a suitable platform for demonstration.

The heterogeneity-graded FGM was fabricated by annealing a long bulk amorphous ribbon under a spatially graded annealing condition established inside a horizontal furnace (see setup photograph in Fig. S1). The initial amorphous ribbon was prepared by the melt-spinning method and cut into ~130 mm in length (4. Experimental Section). The furnace consisted of two temperature zones: a uniform heating zone controlled by PID-controlled heating element

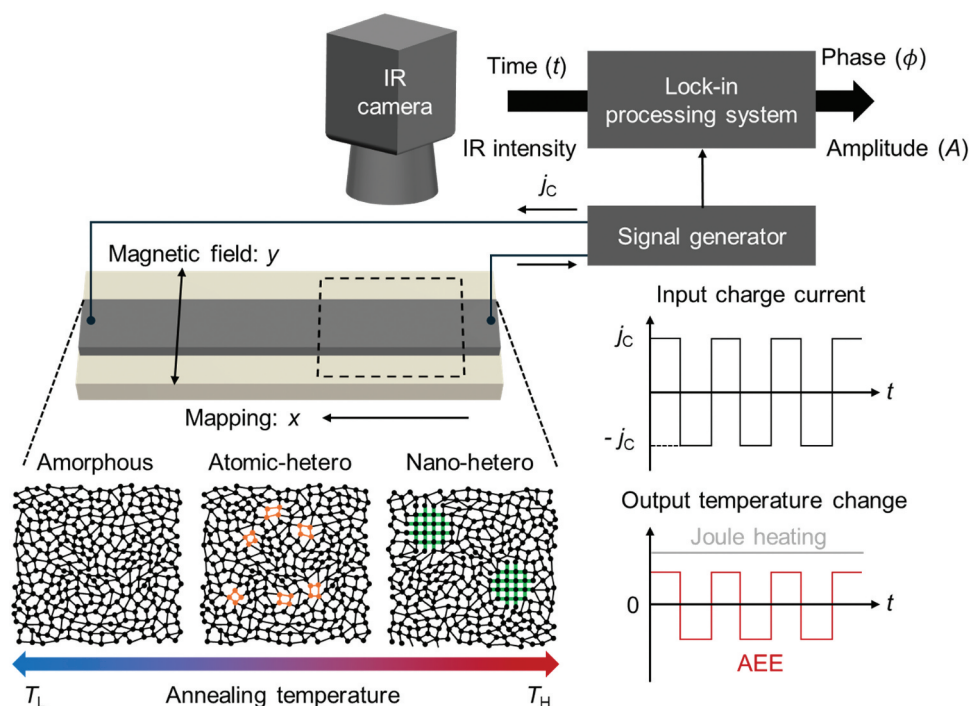


**Figure 1.** Schematic illustration of thermoelectric mapping of a functionally graded material (FGM) with controlled structural heterogeneity using lock-in thermography (LIT). The FGM was fabricated by annealing under a temperature gradient, producing a one-dimensional heterogeneity-graded structure along the sample length (along  $x$ ). LIT scans the sample using a square-wave-modulated input charge current  $j_c$ , enabling spatially resolved detection of the temperature modulation induced by the anomalous Ettingshausen effect (AEE). The magnetic field is applied along  $y$ .



and a cooling zone maintained by a fan, which also protected the O-ring joint used for vacuum sealing. When the heating zone was set to an elevated temperature, a spatial variation in thermal exposure was imposed between the two zones. The annealing was performed under high vacuum ( $<10^{-4}$  Pa) to prevent oxidation. One end of the ribbon was placed in the heating zone and the other in the cooling zone, resulting in a monotonic variation of the annealing condition along its length, which led to a continuous gradient of structural heterogeneity. We note that the formation of the heterogeneity-graded structure was confirmed to be reproducible across multiple independently fabricated ribbons processed under the same furnace configuration (see 4. Experimental Section for details).

The temperature range for annealing was determined based on differential scanning calorimetry (DSC). The DSC data in Fig. S2 show two exothermic peaks during heating at approximately 711 K and 847 K, corresponding to crystallization events. Based on this, the heating zone temperature was set to 773 K, which produces a broad range of structural states from the amorphous on cooling-zone side to partially crystalline on heating-zone side, as illustrated in Figure 1. To enhance cooling and maximize the temperature gradient, the exterior of the cooling zone was covered with a wet cloth (photograph in Fig. S1b). Additional details on the fabrication procedure and experimental setup are provided in 4. Experimental Section. It is

worth noting that although the temperature gradient may not be strictly linear, it remained continuous, producing a continuous gradient of structural states. In the following sections, we examine how this annealing under a temperature gradient influences crystal structures and various material properties, including both longitudinal and transverse transport properties.

## 2.2. Characterization of structural heterogeneity and longitudinal transport properties

We investigated the gradual change in structural heterogeneity using XRD measurements at multiple positions along the sample. The 130 mm-long heterogeneity-graded FGM ribbon was cut to fit the XRD holder. XRD measurements were performed at 10 mm intervals along the sample length to examine the correlation between  $T_a$  and crystallinity. The  $x$ -position in Figure 2 denotes the distance from the low temperature side ( $T_L$ ) to the high temperature side ( $T_H$ ). This positional reference is used consistently throughout all position-dependent data in this study. XRD patterns from the  $T_L$  side ( $x = 5$  mm) exhibit broad peaks in the  $2\theta$  range from  $30$ – $75^\circ$  (based on Cu-K $\alpha_1$  radiation; 4. Experimental Section), indicating a fully amorphous structure (Figure 2(a)). These amorphous features persist up to  $x = 100$  mm, beyond which sharp diffraction peaks corresponding to  $\alpha$ -Fe appear, with negligible evidence of other phases. To quantify the crystallization onset, the full width at half

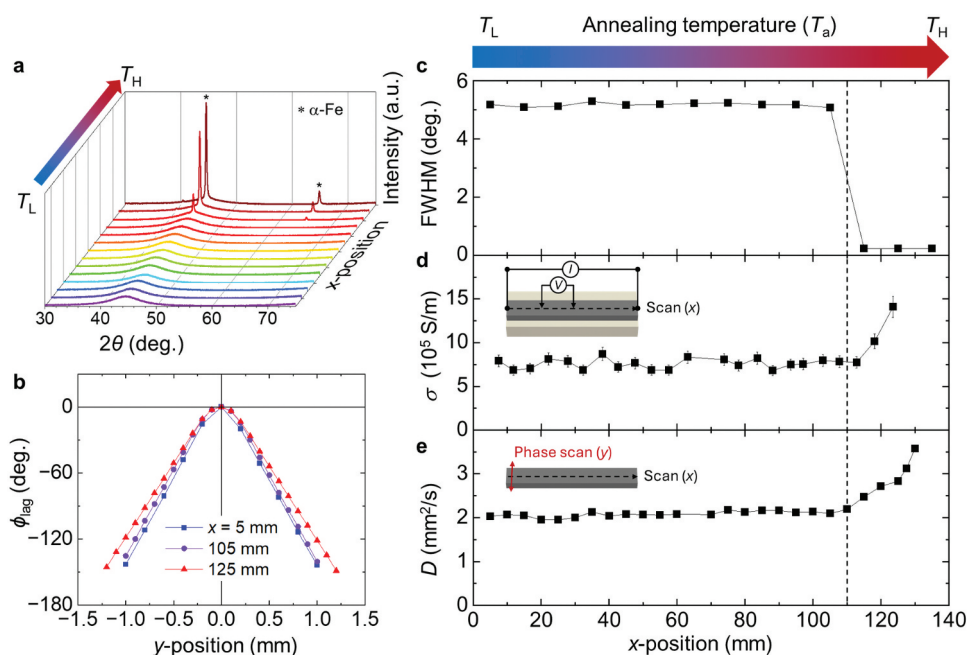


**Figure 2.** Characterization of structural and transport property variations in the heterogeneity-graded FGM ribbon along the length ( $x$ ) direction. (a) X-ray diffraction patterns for various  $x$ -positions. (b) Relative phase lag  $\phi_{lag}$  as a function of  $y$ -position, referenced to the center position ( $y = 0$ ). (c) Full width at half maximum (FWHM) of the main diffraction peak in (a). (d) Longitudinal electrical conductivity ( $\sigma$ ), and (e) thermal diffusivity ( $D$ ), both measured as a function of  $x$  with 5 mm intervals. The FWHM in (c) and  $D$  in (e) were extracted from the data in (a) and (b), respectively. Insets in (d) and (e) illustrate the measurement schematics for electrical and thermal transport characterization. The vertical dashed line in (c)–(e) indicates the crystallization onset.

maximum (FWHM) was extracted from each diffraction pattern and presented in Figure 2(c). A sharp decrease in FWHM begins at approximately  $x = 110$  mm, indicating the onset of crystallization, whereas a small variation is observed across the 0–100 mm region. Beyond this point, the sample exhibits broad amorphous features together with emerging crystalline peaks, indicating partial crystallization from fully amorphous state into amorphous and  $\alpha$ -Fe nanocrystalline phases and the resulting structural heterogeneity (as illustrated in Figure 1). The detailed XRD data are provided in Fig. S3. The structural changes induced by annealing will be discussed in greater detail using STEM and APT measurements in a later section.

We next measured the longitudinal electrical conductivity ( $\sigma$ ) at  $x = 5$  mm intervals using the same samples used for the XRD measurements, where the samples were mounted on glass plates. A standard four-probe method was employed, with two voltage-sensing needle probes scanned along the samples in 5 mm steps, while current electrodes were fixed at both ends (inset, Figure 2(d)). Amorphous phases are known to exhibit lower  $\sigma$  than crystalline phases due to electron localization, and  $\sigma$  increases upon crystallization [40,41]. Figure 2(d) shows that  $\sigma$  remains nearly constant at  $\sim 7.6 \times 10^5$  S/m from  $x = 0$ –110 mm and then increases significantly beyond  $x = 110$  mm, reaching  $14.1 \times 10^5$  S/m at  $x = 125$  mm, consistent with the structural changes observed by XRD.

We then measured the longitudinal thermal diffusivity ( $D$ ). Similar to  $\sigma$ ,  $D$  is expected to be low in the amorphous regime and higher in the crystalline regime due to enhanced heat transport from both lattice and electrons [40–43]. Position-dependent  $D$  was measured using the spot periodic heating radiation thermometry method [59]. In this method, the center of a suspended sample was periodically heated by a laser beam at a frequency  $f$ , inducing thermal oscillations with a finite thermal diffusion length. Given the small sample thickness ( $20 \pm 2$   $\mu$ m), heat diffusion through the thickness (i.e.  $z$ -direction) was assumed to be instantaneous, allowing the heat transfer to be approximated as radial heat flow in the sample plane. Radial heat diffusion was detected using a temperature sensor (4. Experimental Section), which measured both the amplitude and phase lag ( $\phi_{\text{lag}}$ ) of the temperature oscillations relative to the modulated laser input. The phase signal reflects the time delay of heat propagation through the material and was used to extract  $D$  using the following equation [59]:

$$D = \pi f / \left( \frac{d\phi_{\text{lag}}}{dl} \right)^2, \quad (1)$$

where  $l$  is the distance from the thermal excitation center. The phase profile was measured along the  $y$ -direction (see inset, Figure 2(e)), which is orthogonal to the annealing direction ( $x$ ). Material properties are assumed to be spatially uniform due to the absence of a structural heterogeneity gradient in  $y$ . Further details of the measurement are provided in 4. Experimental Section.

Thermal diffusivity was measured at  $x = 5$  mm intervals. Figure 2(b) shows the  $\phi_{\text{lag}}$  profile of the temperature oscillation measured at  $f = 5$  Hz. The slope ( $\frac{d\phi_{\text{lag}}}{dl}$ ) was extracted from the linear regimes in the  $y$ -position ( $\pm 1$  mm to  $\pm 0.25$  mm), and  $D$  was calculated using Equation (1). The symmetric and linear  $\phi_{\text{lag}}$  data confirm negligible variation of thermal properties in the  $y$ -direction, as expected from the one-directional ( $x$ ) temperature gradient during annealing. Figure 2(e) shows that  $D$  remains constant at approximately  $2.1 \text{ mm}^2/\text{s}$  from  $x = 0$  to 110 mm, then increases sharply beyond  $x = 110$  mm, reaching  $2.8 \text{ mm}^2/\text{s}$  at  $x = 125$  mm and  $3.6 \text{ mm}^2/\text{s}$  at  $x = 130$  mm, consistent with increased crystallinity and enhanced lattice and electron contributions [60].

As shown above, XRD, electrical conductivity, and thermal diffusivity measurements consistently show that annealing an amorphous ferromagnetic metal ribbon under a temperature gradient leads to structural and transport property changes detected mainly at the crystallization onset near  $x = 110$  mm, whereas the continuous gradient of structural heterogeneity across the ribbon cannot be resolved by these conventional characterization methods. In the next section, we show that AEE imaging via LIT reveals continuous property variation over a much broader spatial range, highlighting its superior sensitivity to subtle structural heterogeneity.

### 2.3. Spatial mapping of transverse thermoelectric response using LIT

We now present the measurement of the AEE in the heterogeneity-graded FGM sample using LIT with high spatial resolution. A 130-mm-long sample was cut into two halves to apply a magnetic field using an electromagnet, where the sample length should be smaller than the size of the pole pieces. Both ends of the sample were connected to copper wires using silver epoxy and attached to an AC current source. The measurement field-of-view (FOV) was  $7.68 \text{ mm} \times 9.60 \text{ mm}$  for  $512 \times 640$  pixels (327,680 data points in one FOV), providing high-resolution imaging and statistical data points. The entire length of the sample was scanned accordingly, as illustrated in Figure 1.

LIT was performed by applying a square-wave-modulated AC current to the sample under a constant magnetic field ( $H$ ). An IR camera measured

both the lock-in amplitude ( $A$ ) and the phase ( $\phi$ ) of the temperature modulation induced by the applied charge current ( $I$ ). The measured signal includes contributions from multiple effects: the AEE ( $\propto j_C$ ), Peltier effect ( $\propto j_C$ ), and Joule heating ( $\propto j_C^2$ ) contributions, where  $j_C$  is the charge current density. To isolate the thermoelectric contributions, Joule heating was separated by using a zero-offset square-wave-modulated current, which generates a non-oscillating thermal background due to Joule heating without periodic temperature variations (Figure 1). To further extract the pure AEE, the measured data were symmetrized with respect to the magnetic field polarity ( $\pm H$ ). The field-odd components of the amplitude ( $A_{\text{odd}}$ ) and phase ( $\phi_{\text{odd}}$ ) were extracted using the following equations [24,26,27,61–63]:

$$A_{\text{odd}} = \frac{|A_{+H}\exp(-i\phi_{+H}) - A_{-H}\exp(-i\phi_{-H})|}{2}, \quad (2-1)$$

$$\phi_{\text{odd}} = -\arg\left[\frac{(A_{+H}\exp(-i\phi_{+H}) - A_{-H}\exp(-i\phi_{-H}))}{2}\right]. \quad (2-2)$$

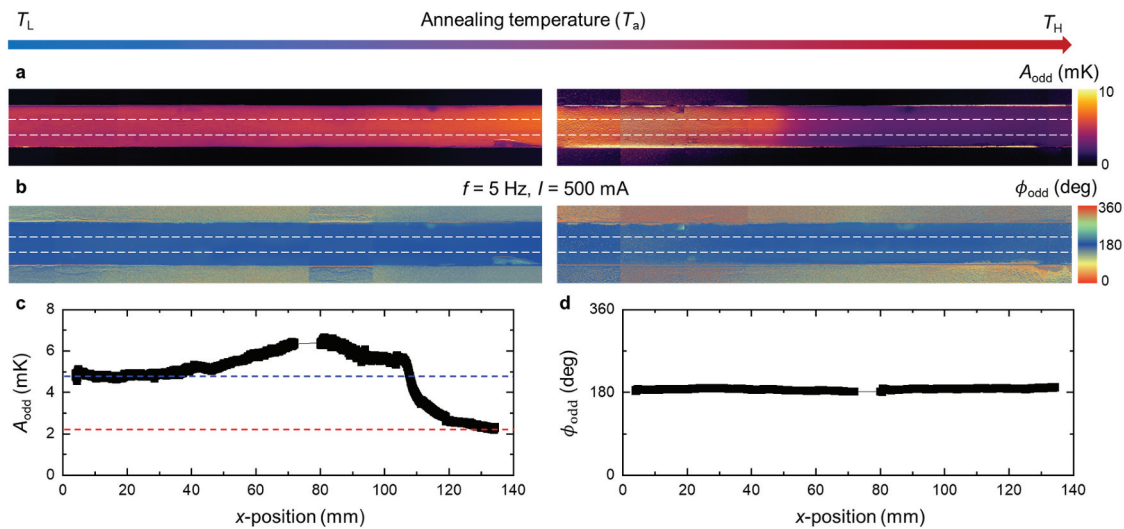
Here,  $A_{\pm H}$  and  $\phi_{\pm H}$  denote the lock-in amplitude and phase under positive ( $+H$ ) and negative ( $-H$ ) magnetic fields, respectively. Note that the magneto-Peltier effect is symmetric with respect to  $H$ , whereas the AEE exhibits field-odd dependence [24,26,27,61–63]. Therefore,  $A_{\text{odd}}$  and  $\phi_{\text{odd}}$  selectively represent the AEE contribution.

Figure 3 presents the spatial mapping of  $A_{\text{odd}}$  and  $\phi_{\text{odd}}$ , measured under an applied current of  $I = 500$  mA and a modulation frequency of  $f = 5$  Hz

(4. Experimental Section). Since the sample thickness remains nearly constant along the ribbon and upon annealing-induced crystallization, the charge current density is identical at all positions under the current-controlled measurement condition. Magnetic fields of  $\pm 0.3$  T were applied along the  $y$ -direction, which is orthogonal to both the sample thickness ( $z$ ) and the current direction ( $x$ ), thereby satisfying the symmetry condition required to detect the AEE using LIT in the  $z$ -direction [27,61–63]. Due to the soft magnetic properties of the sample, with typical coercivity below 0.1 mT [40,42], the entire sample was fully magnetized under the applied  $H$ . The constant values of  $\phi_{\text{odd}}$  in Figure 3(b) confirm that the sample was uniformly magnetized along the  $y$ -direction without noticeable misalignment, validating that the signals represent the pure AEE contribution.

Figure 3(a) shows that  $A_{\text{odd}}$  varies significantly along the  $x$ -direction, reflecting the spatial gradient in structural heterogeneity. In contrast, negligible variation is observed along the  $y$ -direction, indicating that the material properties change predominantly along  $x$ . This behavior is consistent with the one-dimensional temperature gradient imposed by the horizontal furnace (Figure 1), further supporting the reliability of estimating  $D$  from the  $y$ -directional  $\phi_{\text{lag}}$  (Figure 2(b)).

To clarify the  $x$ -directional evolution of the transverse thermoelectric response, we extracted the  $A_{\text{odd}}$  values near the center region of the samples (highlighted by the horizontal white dashed lines in Figure 3(a)) to minimize the warping artifacts. The resulting profile is shown in Figure 3(c). Notably,  $A_{\text{odd}}$  exhibits a non-monotonic profile: it increases steadily from  $x = 0$  mm (4.90 mK), peaks at  $x = 70$ – $80$  mm (6.65 mK),



**Figure 3.** Thermoelectric mapping for a heterogeneity-graded amorphous alloy using lock-in thermography. (a)–(b) Spatial maps of (a) the field-odd lock-in amplitude ( $A_{\text{odd}}$ ) and (b) the corresponding field-odd phase ( $\phi_{\text{odd}}$ ). (c)–(d) averaged line profiles of (c)  $A_{\text{odd}}$  and (d)  $\phi_{\text{odd}}$  along  $x$ -direction, extracted from the highlighted regions in (a) and (b), respectively. The input current was modulated at a frequency  $f = 5$  Hz and amplitude  $I = 500$  mA. The horizontal dashed lines in (c) indicate the properties at  $x = 5$  mm and 130 mm. The applied magnetic field was  $\pm 0.3$  T.

and then decreases gradually, reaching 2.29 mK at  $x = 130$  mm. This profile highlights the spatial evolution and relative enhancement of the field-odd AEE signal along the ribbon. Such continuous variation clearly demonstrates the presence of a gradient in structural heterogeneity along the  $x$ -direction over a wide spatial range. This continuous variation clearly demonstrates the existence of a structural heterogeneity gradient along the  $x$ -direction across a wide range of  $x$ . A steep drop occurs at  $x = 105$  mm, corresponding to the crystallization onset of  $\alpha$ -Fe (Figure 2(a)). Since  $\alpha$ -Fe is known to exhibit small transverse thermoelectric conversion [64], this structural transition explains the sharp drop. The corresponding  $\phi_{\text{odd}}$  profile remains nearly constant at  $180^\circ$  across the sample, with small fluctuations of  $\pm 2^\circ$  (Figure 3(d)), indicating that the sign of the AEE signal is unchanged, consistent with previous observations [40,42]. The absence of data near  $x = 75$  mm in Figure 3(c,d) is due to the inability to measure AEE signals in the electrode regions used for current injection. The field-even amplitude  $A_{\text{even}}$  and phase  $\phi_{\text{even}}$ , which represent spin-independent background contributions, including the Peltier effects, are shown in Fig. S4. These signals are much smaller than the field-odd component over the entire  $x$  range. At the lock-in frequency used in this study (5 Hz), heat losses due to convection and radiation have been shown to be negligible and do not affect the measured LIT amplitude [21].

This non-monotonic trend clearly highlights the unique behavior of the transverse thermoelectric properties compared to the longitudinal transport properties. In the broad region of  $x = 40$ – $105$  mm, the AEE response is higher than that in the amorphous ( $T_L$ ) and crystalline ( $T_H$ ) regimes. Since both longitudinal electrical and thermal transport properties remain nearly constant before crystallization ( $x < 110$  mm), this enhancement directly indicates the presence of additional mechanisms driving transverse electron deflection. In addition, position-dependent magnetization measurements show that the saturation magnetization remains nearly constant throughout the pre-crystallization region ( $x < 110$  mm) and increases slightly for  $x > 110$  mm upon crystallization (see Fig. S5), supporting the conclusion that variations in bulk magnetic ordering or magnetic phase formation are not the primary origin of the observed AEE variation. These mechanisms are likely linked to the gradual evolution of structural heterogeneity in the heterogeneity-graded FGM sample. Previous studies have reported enhanced transverse thermoelectric conversion in Fe-based ferromagnetic amorphous alloys annealed at mid temperatures near the crystallization temperature without strong correlation with chemical composition [42]. Such enhancements have been observed experimentally in ANE and AEE [40,42,43] as well as in the anomalous Hall effect (AHE) [41], with a theoretical model describing the electron paths in complex disordered materials

[41]. In this context, the enhancement reported in [42], established through a high-throughput analysis of more than 150 samples annealed under uniform annealing conditions, indicates that the AEE enhancement observed in the present study originates from the structural state itself and is not attributable to thermal history artifacts associated with temperature gradients. The proposed mechanisms include: (1) the formation of amorphous-crystalline heterostructures [41,43], (2) enhanced spin-orbit coupling (SOC) induced by Cu nanoclusters [40,42], and (3) subtle atomic-scale disorder within the amorphous matrix [42]. These mechanisms are interrelated and collectively suggest the importance of controlling structural heterogeneity at both atomic and nanoscale dimensions in transverse transport. Our observation that the AEE maximum occurs at  $x = 70$ – $80$  mm, well before the crystallization onset ( $x = 110$  mm), suggests that the enhancement in  $T_M$  is associated with the mechanisms of (2) Cu nanoclusters. This interpretation is further supported by bright field (BF)-STEM and APT analyses as discussed in the next section. Furthermore, this enhancement in  $x = 40$ – $105$  mm could not be captured by conventional characterization techniques such as XRD or longitudinal transport measurements (shown in Figure 2), demonstrating that transverse thermoelectric effects are exceptionally sensitive to subtle structural change.

#### 2.4. Structural analyses based on STEM and APT

To clarify the origin of the enhanced AEE observed between  $x = 40$ – $105$  mm (Figure 3(c)), we performed detailed structural analyses using BF-STEM and APT. Three representative positions were selected at  $x = 5$  mm, 80 mm, and 125 mm, corresponding to the amorphous ( $T_L$ ), structurally intermediate ( $T_M$ ), and crystalline ( $T_H$ ) regimes with distinct AEE responses.

The STEM results in Figure 4(a,c) show that the  $T_L$  sample exhibits a fully amorphous phase, as evidenced by the ring-type diffraction patterns in the inset. In contrast, the  $T_H$  sample exhibits mixed amorphous and Fe-crystalline phases, revealing pronounced nanoscale structural heterogeneity. These observations are consistent with the position-dependent XRD results (Figures 2(a) and S3). The  $T_M$  sample ( $x = 80$  mm) appears amorphous without a distinct contrast in structural features compared with the  $T_L$  sample (Figure 4(b)). It should be noted that when the characteristic length scale of such heterogeneity is much smaller than the STEM specimen thickness (tens of nanometers), these nonperiodic features are difficult to resolve directly by STEM.

To capture this hidden structural information, we performed APT on the  $T_M$  sample to probe three-dimensional chemical distributions (4. Experimental Section). The APT results in Figure 4(d) revealed the formation of Cu nanoclusters with an average diameter of 1.7 nm and a number density of  $2.55 \times 10^{23} \text{ m}^{-3}$ ,



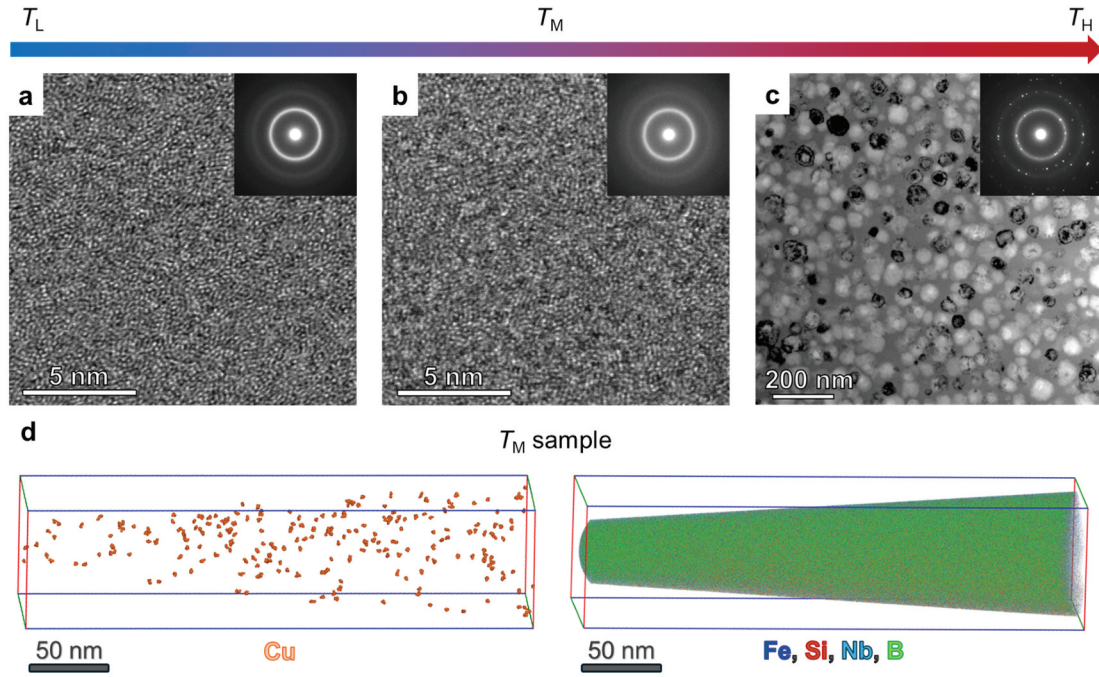


**Figure 4.** Structural characterization of heterogeneity-graded amorphous ribbons using scanning transmission electron microscopy (STEM) and atomic probe tomography (APT). Bright field (BF)-STEM images taken from the samples in (a) low-temperature ( $T_L$ ,  $x = 5$  mm), (b) mid-temperature ( $T_M$ ,  $x = 80$  mm), and (c) high-temperature ( $T_H$ ,  $x = 125$  mm) regimes. (d) Three-dimensional atomic distribution map of constituent elements obtained from  $T_M$  sample by APT.

whereas the other constituent elements (i.e. Fe, Si, Nb, and B) remained uniformly distributed. This indicates the presence of atomic-scale heterogeneity, consistent with our previous observations from discrete sample sets [40,43]. The emergence of these Cu nanoclusters may locally break inversion symmetry at the interfaces with the ferromagnetic Fe-based host matrix, thereby inducing interfacial Rashba-like SOC and generating asymmetric skew scattering [40,42]. This additional interfacial scattering channel enhances transverse thermoelectric conversion, providing a microscopic origin for the increased AEE in the  $T_M$  regime.

## 2.5. Discussion on the origin of enhanced transverse thermoelectric conversion

To elucidate the origin of enhanced transverse signal, we evaluate the anomalous Nernst conductivity ( $\alpha_{ANE}$ ) as a fundamental transport coefficient governing transverse thermoelectricity. The anomalous Ettingshausen coefficient determined experimentally is

$$\Pi_{AEE} = \frac{\pi \kappa \Delta T_{AEE}}{4 j_c t}, \quad (3)$$

where  $\Delta T_{AEE}$  is the magnitude of  $\Delta T$  induced by AEE along the  $z$ -direction (i.e.  $\Delta T_{AEE} = 2A_{odd}$ ),  $j_c$  is the longitudinal charge-current density,  $t$  is the sample thickness, and  $\kappa$  is the thermal conductivity

[40,42,43]. The anomalous Nernst conductivity is expressed as

$$\alpha_{ANE} = \sigma_{xx}(S_{ANE} + \theta_{AHE}S_{xx}), \quad (4)$$

where  $S_{ANE}$  is the anomalous Nernst coefficient,  $S_{xx}$  is the Seebeck coefficient, and  $\theta_{AHE}$  ( $=\sigma_{AHE}/\sigma_{xx}$ ) is the anomalous Hall angle with  $\sigma_{AHE}$  being the anomalous Hall conductivity. The Onsager reciprocal relation connects the two effects as [40,42,43]

$$\Pi_{AEE} = TS_{ANE}. \quad (5)$$

where  $T$  is the absolute temperature, leading to

$$\alpha_{ANE} = \sigma_{xx}(\Pi_{AEE}/T + \theta_{AHE}S_{xx}). \quad (6)$$

The first term ( $\sigma_{xx}\Pi_{AEE}/T$ ) represents the ANE-related intrinsic transverse thermoelectric contribution, whereas the second term ( $\sigma_{xx}\theta_{AHE}S_{xx}$ ) corresponds to the Hall-deflected Seebeck contribution. Here, the term ‘intrinsic’ denotes a material specific transport property governed by  $S_{ANE}$  or  $\Pi_{AEE}$ , which should be distinct from intrinsic Berry curvature vs. extrinsic (skew/side-jump) classifications of microscopic mechanisms discussed elsewhere [34–39].

We compare these two contributions in Equation (6) by inserting the experimentally measured  $\Pi_{AEE}$ ,  $\sigma_{AHE}$  (hence  $\theta_{AHE}$ ), and  $S_{xx}$  (4. Experimental Section). By assuming negligible ordinary contributions (i.e. ordinary Nernst and Ettingshausen effects), as supported by previous studies reporting minor field-dependent components in amorphous alloys [41], we evaluate  $\alpha_{ANE}$  as

a fundamental transport coefficient. Following the STEM and APT analyses, we select three representative positions for comparison:  $T_L$ ,  $T_M$ , and  $T_H$ . Figure 5 summarizes the transport parameters:  $\sigma_{\text{AHE}}$  increases towards  $T_H$  mainly due to enhancement of  $\sigma_{xx}$ , whereas  $S_{xx}$  remains nearly constant at approximately  $-1.3 \mu\text{V/K}$  across the samples. To quantify the relative contributions, we define a dominance ratio

$$R \equiv \left| \frac{\sigma_{xx} \Pi_{\text{AEE}}/T}{\sigma_{xx} \theta_{\text{AHE}} S_{xx}} \right| = \left| \frac{\Pi_{\text{AEE}}/T}{\theta_{\text{AHE}} S_{xx}} \right|. \quad (7)$$

Across  $T_L$ ,  $T_M$ , and  $T_H$ , we obtain  $R > 25$  (i.e. the contribution of the Hall-deflected Seebeck term is  $<4\%$ , as shown in Figure 5(c), demonstrating that the observed enhancement is dominated by the ANE-related term  $\sigma_{xx} \Pi_{\text{AEE}}/T$ , while the  $\theta_{\text{AHE}} S_{xx}$  channel is negligible.

Figure 5(c) shows that the resulting  $\alpha_{\text{ANE}}$  increases monotonically from  $T_L$  (1.30 A/mK) to  $T_M$  (1.83 A/mK) and peaks at  $T_H$  (2.39 A/mK). This peak value exceeds the maximum value reported for discrete sample sets with similar compositions (up to 1.93 A/mK) in previous studies [40], clearly demonstrating the effectiveness of our strategy integrating FGM with LIT. The enhanced  $\alpha_{\text{ANE}}$  in  $T_H$  is attributable to the nanoscale amorphous-crystalline heterostructure (as observed by STEM in Figure 4c and XRD in Fig. S3), which may induce asymmetric carrier scattering, consistent with the recently reported composite-transport model in Ref [41].

## 2.6. Mechanical flexibility of heterogeneity-graded ribbon

Another promising functionality of amorphous alloys is their mechanical flexibility, which allows transverse thermoelectric energy conversion from curved heat sources, for example using coiled structures as proposed and demonstrated in [43,56,65,66]. This versatility broadens the applicability of the materials to diverse device architectures. It is also well established that mechanical ductility is strongly dependent on the

crystallinity of the system [40,41,43]. For example, Park et al. reported that the maximum bending radius of amorphous metals increases significantly when the samples are annealed at high temperatures, which was explained by the reduction of ductile amorphous fractions and the growth of rigid crystalline fractions within the composite matrix [43]. Therefore, achieving high transverse thermoelectric performance while retaining mechanical flexibility is of great importance for the development of flexible transverse thermoelectric materials.

To further examine the mechanical properties of the heterogeneity-graded FGM ribbon, we attached the sample to a curved surface with a radius of 5 mm. The same samples used for the thermal diffusivity measurement were employed for this mechanical test. Figure S6 shows that the overall sample retained its mechanical flexibility. However, the  $x > 110$  mm region fractured during handling due to the brittle crystalline phases, confirmed by XRD (Figure 2) and STEM (Figure 4). This result qualitatively demonstrates that the high-performing amorphous-to-nano-heterogeneity region of the FGM is applicable to devices that require mechanical flexibility.

## 3. Conclusion

We demonstrated a simple and scalable strategy to fabricate heterogeneity-graded amorphous alloy ribbons by annealing under a one-dimensional temperature gradient. This approach provides a unique experimental platform to systematically investigate the relationship between structural heterogeneity and transverse thermoelectric conversion. By employing LIT with high spatial and temperature resolution, we directly mapped the AEE along the heterogeneity gradient and revealed a pronounced non-monotonic response of AEE-induced temperature modulation under a constant electrical current. Detailed STEM and APT analyses confirmed that this enhancement originates from nanoscale structural heterogeneity of Fe-based alloys and Cu nanoclusters within the

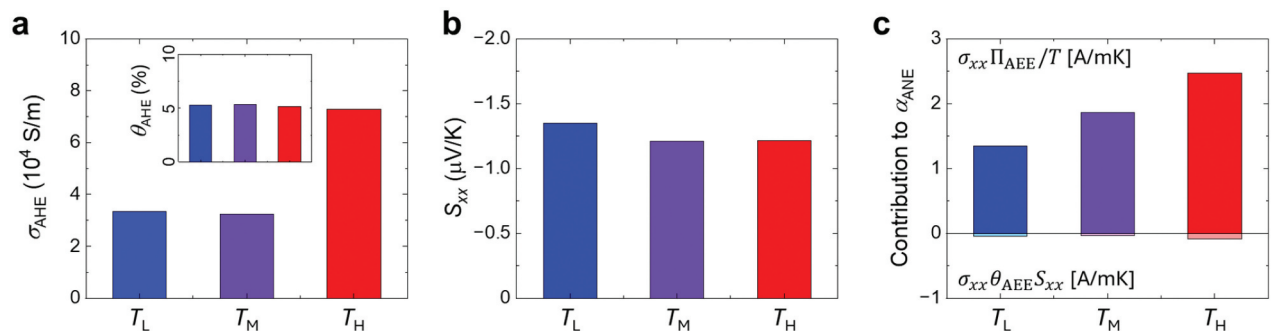


**Figure 5.** Transport properties of the three representative samples at  $T_L$  ( $x = 5$  mm),  $T_M$  ( $x = 80$  mm), and  $T_H$  ( $x = 125$  mm). (a) Anomalous Hall conductivity ( $\sigma_{\text{AHE}}$ ) and anomalous Hall angle ( $\theta_{\text{AHE}}$ , inset), (b) Seebeck coefficient ( $S_{xx}$ ), and (c) decomposition of the anomalous Nernst conductivity  $\alpha_{\text{ANE}}$  into the two contributing terms.

amorphous matrix. Importantly, these critical features could not be detected by conventional characterization methods such as lab-scale XRD or longitudinal transport measurements, underscoring the exceptional sensitivity of transverse thermoelectric phenomena to subtle structural variations. Furthermore, the high-performing amorphous-to-nano-heterogeneous region of the FGM ribbon retains its mechanical flexibility, supporting its applicability in flexible device architectures. Overall, this work establishes heterogeneity-graded FGMs combined with LIT imaging as a powerful, high-throughput, and highly sensitive methodology to study the role of structural heterogeneity in transverse electron transport. Rather than targeting a specific annealing condition that maximizes the transverse thermoelectric response, the present study demonstrates how a continuous evolution of atomic- and nano-scale structural heterogeneity gives rise to a pronounced maximum in the AEE signal within a single functionally graded amorphous ribbon. Beyond advancing the fundamental understanding of heterogeneity-driven thermoelectric phenomena, our results highlight a practical route for designing flexible materials and devices with enhanced transverse thermoelectric performance.

## 4. Experimental section

### 4.1. Preparation of initial homogeneous amorphous ribbons

Master alloy ingots were synthesized by melting a mixture of high-purity elemental constituents in a high-frequency induction furnace under an argon atmosphere. The resulting ingots were crushed into small fragments and loaded into a quartz tube equipped with a 5.0 mm × 0.8 mm nozzle. Amorphous ribbons were fabricated using a single-roll melt-spinning process, in which the ingot fragments were re-melted via induction heating and the molten alloy was ejected through the nozzle under an argon atmosphere at a pressure of 0.04 MPa onto a copper wheel rotating at 30 m/s. The nozzle-to-wheel gap was maintained at 0.2 mm throughout the process. The thickness of the ribbon was measured to be  $20 \pm 2 \mu\text{m}$  using a micrometer.

### 4.2. Fabrication of heterogeneity-graded amorphous ribbons

Heterogeneity-graded amorphous ribbons were fabricated by annealing homogeneous amorphous ribbons under a temperature gradient naturally established within a horizontal tube furnace. The furnace consisted of a heating zone equipped with a resistive heating element and a cooling zone assisted by a fan (see Fig. S1 for the setup). The

ribbon was cut to a length of approximately 130 mm, with one end placed in the heating zone and the other in the cooling zone. This configuration imposed a monotonic spatial variation of thermal exposure along the ribbon length (i.e.  $x$ -direction), leading to a gradual gradient of structural heterogeneity. Such a structure provides a suitable platform for investigating the influence of crystallinity and atomic-scale structural heterogeneity on transverse thermoelectric conversion. Multiple heterogeneity-graded ribbons were independently fabricated using the same furnace configuration and annealing protocol, and all independently fabricated ribbons consistently exhibited a crystallinity-induced structural and property transition at approximately the same position along the ribbon length. This reproducibility indicates that the imposed boundary condition for forming the graded structure is well defined and stable (Fig. S1). For subsequent characterization, three independently fabricated ribbons were used as follows: (i) one ribbon for LIT imaging (Figure 3) together with TEM and APT analysis (Figure 4), (ii) a second ribbon for electrical conductivity (Figure 2(d)) and XRD measurements (Figure 2(a)), and (iii) a third ribbon for thermal diffusivity (Figure 2(e)) and mechanical testing (Fig. S6).

The annealing condition along the ribbon length was governed by the temperature difference between the heating and cooling zones, which were independently controlled by the furnace and fan-assisted cooling, respectively. The heating zone temperature was maintained at 773 K using the heating element, while the cooling zone temperature was kept near room temperature by a fan-assisted forced convection, with a wet cloth used to enhance thermal dissipation. The heating zone temperature increased at a ramp rate of 10 K/min, held at the set temperature for 15 min, and then cooled naturally. All heat treatments were performed under high vacuum ( $<10^{-5}$  Pa) to prevent oxidation.

### 4.3. Characterization of crystallinity using DSC

Structural transitions associated with exothermic reactions were examined using DSC (Rigaku, Thermo plus EVO2). Measurements were carried out in a platinum crucible over a temperature range of 273–993 K at a heating rate of 10 K/min. Prior to the measurements, the samples were preheated at 373 K for 10 min to remove any residual moisture.

### 4.4. Characterization of change in structural heterogeneity using XRD

Structural characterization was carried out using a Rigaku MiniFlex600 X-ray diffractometer equipped



with a Cr-K $\alpha$  source ( $\lambda = 0.22897$  nm). For consistency in comparison, the diffraction angles were converted to the commonly used Cu-K $\alpha$  equivalent ( $\lambda = 0.15406$  nm), as presented in [Figures 2](#) and [S3](#). The X-ray tube was operated at 40 kV and 15 mA.  $\theta$ - $2\theta$  scans were performed sequentially at 10 mm intervals along the  $x$ -position of the ribbon length.

#### 4.5. Measurement of position-dependent electrical conductivity

The electrical conductivity ( $\sigma$ ) of the sample was mapped using a standard four-probe method using a digital multimeter (Keithley, DMM6500). The four electrodes were connected using a probe scanning system equipped with needle probes. Specifically, two electrodes to apply a charge current were attached at both ends of the sample using silver epoxy in a line-contact configuration, ensuring uniform current flow along the sample length. Position-dependent voltage measurements were obtained using two point-contact probes, which were sequentially scanned along the sample. The sample was mounted on a rigid glass substrate, consistent with the setup used for XRD measurement.

#### 4.6. Measurement of position-dependent thermal diffusivity

The thermal diffusivity ( $D$ ) of the heterogeneity-graded FGM sample was measured using the spot periodic heating radiation thermometry method [\[59\]](#). The sample was suspended between a modulated laser source (top) and an IR temperature detection system (bottom), with alignment maintained using a linear motor stage. The center of the suspended sample was periodically heated by a laser beam with a wavelength of 808 nm and a beam diameter of 150  $\mu$ m. The laser was square-wave-modulated at a frequency of 5 Hz with a 50% duty cycle, resulting in an average power of 1.4 mW.

The resulting spatial heat diffusion was detected on the rear side of the specimen using the temperature detection system. Specifically, thermal radiation was collected using a Ge lens, and the temperature oscillations at each position were measured using an InSb IR detector cooled with liquid nitrogen. The phase lag between the modulated heating signal and the detected temperature response was analyzed using a lock-in amplifier. The values of  $D$  were estimated using the phase lag in [Figure 2\(b\)](#) and Equation (1).

#### 4.7. LIT-based AEE mapping

The spatial distribution of AEE was characterized using a LIT system (DCG Systems Inc., ELITE). The samples were fixed onto a glass substrate using an electrically insulating adhesive. Measurements were

conducted by applying a square-wave-modulated charge current with an amplitude of 500 mA under an in-plane magnetic field ( $y$ -direction) of  $\pm 0.3$  T at room temperature ( $T = 300$  K). The details of the measurements are described in Ref [\[40,42,43\]](#).

#### 4.8. Structural analysis via APT and STEM

Microstructural analysis was conducted using a FEI Titan G2 80–200 TEM. Elemental distribution was observed using APT in a laser mode with a CAMECA LEAP 5000 XS instrument, operated at a base temperature of 30 K and a laser pulse rate and energy of 250 KHz and 30 pJ, respectively. APT and STEM specimens were prepared using the lift-out technique with a FEI Helios 5UX dual beam-focused ion beam. APT data analysis was performed using CAMECA AP Suite 6.3 software.

#### 4.9. Position-dependent magnetization measurement

The magnetic properties were measured using a SQUID-VSM (MPMS3). The sample was cut into segments at 10 mm intervals, and magnetization measurements were performed at each position. The magnetic field was swept between  $\pm 0.1$  T with a field step of 0.1 mT. All measurements were conducted at room temperature ( $T = 300$  K).

#### 4.10. Measurement of anomalous hall conductivity and Seebeck coefficient

The anomalous Hall effect of the three representative samples was measured using a DC resistivity probe integrated in a He cryostat (Cryogenics, CFMS). Standard four-probe measurements were conducted with a current source (Keithley, 2450) and a nanovoltmeter (Keithley, 2182A). A linear voltage-current response was confirmed by measuring 5 points with opposite current polarities. The Seebeck coefficient was measured at room temperature using a ZEM-3 system (ADVANCE RIKO).

#### Author contributions

S.J.P. designed and conceived the study. K.U. supervised the project. R.G. and H.S.A. fabricated the initial as-spun amorphous metals, performed APT and TEM measurements, and analyzed the corresponding data. S.J.P. fabricated the heterogeneity-graded amorphous metals, measured and analyzed the XRD, DSC, Hall, Seebeck data, and performed the LIT measurements and analysis. S.J.P. and R.M. measured position-dependent electrical resistivity. S.J.P. measured and analyzed the position-dependent thermal diffusivity with help



from Y.T. S.J.P. wrote the manuscript with contributions from all authors.

## Acknowledgments

The authors thank M. Goto for valuable discussion.

## Disclosure statement

No potential conflict of interest was reported by the author(s).

## Funding

This work was supported by Japan Science and Technology Agency (JST), ERATO Magnetic Thermal Management Materials project [grant no. JPMJER2201].

## ORCID

Sang J. Park  <http://orcid.org/0000-0003-1684-4876>  
 Ravi Gautam  <http://orcid.org/0000-0002-5442-6328>  
 Takashi Yagi  <http://orcid.org/0000-0002-2008-872X>  
 Rajkumar Modak  <http://orcid.org/0000-0001-7939-3289>  
 Hossein Sepehri-Amin  <http://orcid.org/0000-0002-7856-7897>  
 Ken-ichi Uchida  <http://orcid.org/0000-0001-7680-3051>

## Data availability statement

The data that support the findings of this study are available from the corresponding authors upon reasonable request.

## References

- [1] Koizumi M. FGM activities in Japan. *Compos Part B Eng.* 1997;28(1–2):1–4. doi: [10.1016/S1359-8368\(96\)00016-9](https://doi.org/10.1016/S1359-8368(96)00016-9)
- [2] Naebe M, Shirvanimoghaddam K. Functionally graded materials: a review of fabrication and properties. *Appl Mater Today.* 2016;5:223–245. doi: [10.1016/j.apmt.2016.10.001](https://doi.org/10.1016/j.apmt.2016.10.001)
- [3] Li Y, Feng Z, Hao L, et al. A review on functionally graded materials and structures via additive manufacturing: from multi-scale design to versatile functional properties. *Adv Mater Technol.* 2020;5(6):1900981. doi: [10.1002/admt.201900981](https://doi.org/10.1002/admt.201900981)
- [4] Zhang C, Chen F, Huang Z, et al. Additive manufacturing of functionally graded materials: a review. *Mater Sci Eng A.* 2019;764:138209. doi: [10.1016/j.msea.2019.138209](https://doi.org/10.1016/j.msea.2019.138209)
- [5] Jha DK, Kant T, Singh RK. A critical review of recent research on functionally graded plates. *Compos Struct.* 2013;96:833–849. doi: [10.1016/j.compstruct.2012.09.001](https://doi.org/10.1016/j.compstruct.2012.09.001)
- [6] Cannillo V, Lusvarghi L, Siligardi C, et al. Prediction of the elastic properties profile in glass–alumina functionally graded materials. *J Eur Ceram Soc.* 2007;27(6):2393–2400. doi: [10.1016/j.jeurceramsoc.2006.09.009](https://doi.org/10.1016/j.jeurceramsoc.2006.09.009)
- [7] Hedegaard EMJ, Mamakhel AAH, Reardon H, et al. Functionally graded  $(\text{PbTe})_{1-x}(\text{SnTe})_x$  thermoelectrics. *Chem Mater.* 2018;30(1):280–287. doi: [10.1021/acs.chemmater.7b04473](https://doi.org/10.1021/acs.chemmater.7b04473)
- [8] Niu W, Cao X, Hu Y, et al. Analytical analysis of temperature-dependent thermoelectric generator and optimization based on functionally graded materials. *Int J Energy Res.* 2022;46(15):23963–23972. doi: [10.1002/er.8693](https://doi.org/10.1002/er.8693)
- [9] Han H, Yang SE, Lee J, et al. 3D-printed functionally graded thermoelectric materials for enhanced power generation. *Chem Eng J.* 2024;497:154547. doi: [10.1016/j.cej.2024.154547](https://doi.org/10.1016/j.cej.2024.154547)
- [10] Kumar S, Murthy Reddy KVVS, Kumar A, et al. Development and characterization of polymer–ceramic continuous fiber reinforced functionally graded composites for aerospace application. *Aerosp Sci Technol.* 2013;26(1):185–191. doi: [10.1016/j.ast.2012.04.002](https://doi.org/10.1016/j.ast.2012.04.002)
- [11] Wang Y, Sakai A, Minami S, et al. Robust giant anomalous Nernst effect in polycrystalline nodal web ferromagnets. *Appl Phys Lett.* 2024;125(8):081901. doi: [10.1063/5.0219416](https://doi.org/10.1063/5.0219416)
- [12] Feng Z, Minami S, Akamatsu S, et al. Giant and robust anomalous Nernst effect in a polycrystalline topological ferromagnet at room temperature. *Adv Funct Mater.* 2022;32(49):2206519. doi: [10.1002/adfm.202206519](https://doi.org/10.1002/adfm.202206519)
- [13] Park SJ, Cao Van P, Kang MG, et al. Enhancing spin pumping by nonlocal manipulation of magnon temperature. *Matter.* 2024;7(12):4332–4341. doi: [10.1016/j.matt.2024.08.023](https://doi.org/10.1016/j.matt.2024.08.023)
- [14] Kim MY, Park SJ, Kim GY, et al. Designing efficient spin Seebeck-based thermoelectric devices via simultaneous optimization of bulk and interface properties. *Energy Environ Sci.* 2021;14(6):3480–3491. doi: [10.1039/D1EE00667C](https://doi.org/10.1039/D1EE00667C)
- [15] Kim MY, Lee D, Lee JH, et al. Oxygen vacancy defect engineering for transverse thermoelectric enhancement: a novel extrinsic pathway beyond intrinsic approaches. *Adv Sci.* 2025;12(27):2502892. doi: [10.1002/advs.202502892](https://doi.org/10.1002/advs.202502892)
- [16] Hirayama Y, Iguchi R, Miao XF, et al. High-throughput direct measurement of magnetocaloric effect based on lock-in thermography technique. *Appl Phys Lett.* 2017;111(16):163901. doi: [10.1063/1.5000970](https://doi.org/10.1063/1.5000970)
- [17] Nakajima H, Morimoto T, Okigawa Y, et al. Imaging of local structures affecting electrical transport properties of large graphene sheets by lock-in thermography. *Sci Adv.* 2019;5(2):eaau3407. doi: [10.1126/sciadv.aau3407](https://doi.org/10.1126/sciadv.aau3407)
- [18] Bang KM, Park W, Ziolkowski P, et al. Fabrication and cooling performance optimization of stretchable thermoelectric cooling device. *ACS Appl Electron Mater.* 2021;3(12):5433–5442. doi: [10.1021/acsaem.1c00886](https://doi.org/10.1021/acsaem.1c00886)
- [19] Park SJ, Bang KM, Kim B, et al. Adaptive thermoelectric cooling system for energy-efficient local and transient heat management. *Appl Therm Eng.* 2022;216:119060. doi: [10.1016/j.applthermaleng.2022.119060](https://doi.org/10.1016/j.applthermaleng.2022.119060)
- [20] Park SJ, Park J, Bang KM, et al. Thermoelectric hot-spot cooling using thermally conductive fillers. *Appl Therm Eng.* 2023;232:120994. doi: [10.1016/j.applthermaleng.2023.120994](https://doi.org/10.1016/j.applthermaleng.2023.120994)
- [21] Alasli A, Miura A, Iguchi R, et al. High-throughput imaging measurements of thermoelectric figure of merit. *Sci Technol Adv Mater Methods.* 2021;1(1):162–168. doi: [10.1080/27660400.2021.1963642](https://doi.org/10.1080/27660400.2021.1963642)

- [22] Straube H, Wagner JM, Breitenstein O. Measurement of the Peltier coefficient of semiconductors by lock-in thermography. *Appl Phys Lett*. 2009;95(5):052107. doi: [10.1063/1.3194156](https://doi.org/10.1063/1.3194156)
- [23] Modak R, Hirai T, Sakuraba Y, et al. High-throughput optimization of magnetoresistance materials based on lock-in thermography. *Adv Phys Res*. 2024;3(8):2400021. doi: [10.1002/apxr.202400021](https://doi.org/10.1002/apxr.202400021)
- [24] Uchida K, Sasaki M, Sakuraba Y, et al. Combinatorial investigation of spin-orbit materials using spin Peltier effect. *Sci Rep*. 2018;8(1):16067. doi: [10.1038/s41598-018-34493-6](https://doi.org/10.1038/s41598-018-34493-6)
- [25] Modak R, Goto K, Ueda S, et al. Combinatorial tuning of electronic structure and thermoelectric properties in  $\text{Co}_2\text{MnAl}_{1-x}\text{Si}_x$  Weyl semimetals. *APL Mater*. 2021;9(3):031105. doi: [10.1063/5.0041100](https://doi.org/10.1063/5.0041100)
- [26] Daimon S, Iguchi R, Hioki T, et al. Thermal imaging of spin Peltier effect. *Nat Commun*. 2016;7(1):13754. doi: [10.1038/ncomms13754](https://doi.org/10.1038/ncomms13754)
- [27] Seki T, Iguchi R, Takanashi K, et al. Relationship between anomalous Ettingshausen effect and anomalous Nernst effect in an FePt thin film. *J Phys D Appl Phys*. 2018;51(25):254001. doi: [10.1088/1361-6463/aac481](https://doi.org/10.1088/1361-6463/aac481)
- [28] Uchida K, Daimon S, Iguchi R, et al. Observation of anisotropic magneto-Peltier effect in nickel. *Nature*. 2018;558(7708):95–99. doi: [10.1038/s41586-018-0143-x](https://doi.org/10.1038/s41586-018-0143-x)
- [29] Mizuguchi M, Nakatsuji S. Energy-harvesting materials based on the anomalous Nernst effect. *Sci Technol Adv Mater*. 2019;20(1):262–275. doi: [10.1080/14686996.2019.1585143](https://doi.org/10.1080/14686996.2019.1585143)
- [30] Sakai A, Minami S, Koretsune T, et al. Iron-based binary ferromagnets for transverse thermoelectric conversion. *Nature*. 2020;581(7806):53–57. doi: [10.1038/s41586-020-2230-z](https://doi.org/10.1038/s41586-020-2230-z)
- [31] Pan Y, Le C, He B, et al. Giant anomalous Nernst signal in the antiferromagnet  $\text{YbMnBi}_2$ . *Nat Mater*. 2022;21(2):203–209. doi: [10.1038/s41563-021-01149-2](https://doi.org/10.1038/s41563-021-01149-2)
- [32] Masuda H, Modak R, Seki T, et al. Large spin-Hall effect in non-equilibrium binary copper alloys beyond the solubility limit. *Commun Mater*. 2020;1(1):75. doi: [10.1038/s43246-020-00076-0](https://doi.org/10.1038/s43246-020-00076-0)
- [33] Modak R, Sakuraba Y, Hirai T, et al. Sm–Co-based amorphous alloy films for zero-field operation of transverse thermoelectric generation. *Sci Technol Adv Mater*. 2022;23(1):767–782. doi: [10.1080/14686996.2022.2138538](https://doi.org/10.1080/14686996.2022.2138538)
- [34] Nagaosa N, Sinova J, Onoda S, et al. Anomalous Hall effect. *Rev Mod Phys*. 2010;82(2):1539–1592. doi: [10.1103/RevModPhys.82.1539](https://doi.org/10.1103/RevModPhys.82.1539)
- [35] Sinova J, Valenzuela SO, Wunderlich J, et al. Spin Hall effects. *Rev Mod Phys*. 2015;87(4):1213–1260. doi: [10.1103/RevModPhys.87.1213](https://doi.org/10.1103/RevModPhys.87.1213)
- [36] Xu L, Li X, Ding L, et al. Anomalous transverse response of  $\text{Co}_2\text{MnGa}$  and universality of the room-temperature  $\alpha_{\text{H}}/\sigma_{\text{H}}$  ratio across topological magnets. *Phys Rev B*. 2020;101(18):180404(R). doi: [10.1103/PhysRevB.101.180404](https://doi.org/10.1103/PhysRevB.101.180404)
- [37] Ding L, Koo J, Xu L, et al. Intrinsic anomalous Nernst effect amplified by disorder in a half-metallic semimetal. *Phys Rev X*. 2019;9(4):041061. doi: [10.1103/PhysRevX.9.041061](https://doi.org/10.1103/PhysRevX.9.041061)
- [38] Tian Y, Ye L, Jin X. Proper scaling of the anomalous Hall effect. *Phys Rev Lett*. 2009;103(8):087206. doi: [10.1103/PhysRevLett.103.087206](https://doi.org/10.1103/PhysRevLett.103.087206)
- [39] Hou D, Su G, Tian Y, et al. Multivariable scaling for the anomalous Hall effect. *Phys Rev Lett*. 2015;114(21):217203. doi: [10.1103/PhysRevLett.114.217203](https://doi.org/10.1103/PhysRevLett.114.217203)
- [40] Gautam R, Hirai T, Alasli A, et al. Creation of flexible spin-caloritronic material with giant transverse thermoelectric conversion by nanostructure engineering. *Nat Commun*. 2024;15:2184. doi: [10.1038/s41467-024-46475-6](https://doi.org/10.1038/s41467-024-46475-6)
- [41] Park SJ, Lee H, Lee JM, et al. Electron transverse transport enhancement by composite formation. *Phys Rev Lett*. 2026;136(5):056301. doi: [10.1103/PhysRevLett.136.056301](https://doi.org/10.1103/PhysRevLett.136.056301)
- [42] Park SJ, Gautam R, Alasli A, et al. High-throughput development of flexible amorphous materials showing large anomalous Nernst effect via automatic annealing and thermoelectric imaging. *Mater Today*. 2026;92:416–424. doi: [10.1016/j.mattod.2025.12.027](https://doi.org/10.1016/j.mattod.2025.12.027)
- [43] Park SJ, Modak R, Gautam R, et al. Designing flexible hard magnetic materials for zero-magnetic-field operation of the anomalous Nernst effect. *Acta Mater*. 2025;301:121422. doi: [10.1016/j.actamat.2025.121422](https://doi.org/10.1016/j.actamat.2025.121422)
- [44] Park SJ, Bang KM, Park J, et al. High heat-flux sensitivity of the planar coil device based on the anomalous Nernst effect. *Appl Therm Eng*. 2025;265:125555. doi: [10.1016/j.applthermaleng.2025.125555](https://doi.org/10.1016/j.applthermaleng.2025.125555)
- [45] Correa MA, Ferreira A, Souza ALR, et al. Anomalous Nernst effect in flexible Co-based amorphous ribbons. *Sensors*. 2023;23(3):1420. doi: [10.3390/s23031420](https://doi.org/10.3390/s23031420)
- [46] Asaba T, Ivanov V, Thomas SM, et al. Colossal anomalous Nernst effect in a correlated noncentrosymmetric kagome ferromagnet. *Sci Adv*. 2021;7(13):eabf1467. doi: [10.1126/sciadv.abf1467](https://doi.org/10.1126/sciadv.abf1467)
- [47] Ikhlas M, Tomita T, Koretsune T, et al. Large anomalous Nernst effect at room temperature in a chiral antiferromagnet. *Nat Phys*. 2017;13(11):1085–1090. doi: [10.1038/nphys4181](https://doi.org/10.1038/nphys4181)
- [48] Li M, Pi H, Zhao Y, et al. Large anomalous Nernst effects at room temperature in  $\text{Fe}_3\text{Pt}$  thin films. *Adv Mater*. 2023;35(32):2301339. doi: [10.1002/adma.202301339](https://doi.org/10.1002/adma.202301339)
- [49] He B, Şahin C, Boona SR, et al. Large magnon-induced anomalous Nernst conductivity in single-crystal  $\text{MnBi}$ . *Joule*. 2021;5(11):3057–3067. doi: [10.1016/j.joule.2021.08.007](https://doi.org/10.1016/j.joule.2021.08.007)
- [50] Sakai A, Mizuta YP, Nugroho AA, et al. Giant anomalous Nernst effect and quantum-critical scaling in a ferromagnetic semimetal. *Nat Phys*. 2018;14(11):1119–1124. doi: [10.1038/s41567-018-0225-6](https://doi.org/10.1038/s41567-018-0225-6)
- [51] Guin SN, Manna K, Noky J, et al. Anomalous Nernst effect beyond the magnetization scaling relation in the ferromagnetic Heusler compound  $\text{Co}_2\text{MnGa}$ . *NPG Asia Mater*. 2019;11(1):16. doi: [10.1038/s41427-019-0116-z](https://doi.org/10.1038/s41427-019-0116-z)
- [52] Chen T, Minami S, Sakai A, et al. Large anomalous Nernst effect and nodal plane in an iron-based kagome ferromagnet. *Sci Adv*. 2022;8(2):eabk1480. doi: [10.1126/sciadv.abk1480](https://doi.org/10.1126/sciadv.abk1480)
- [53] Mende F, Noky J, Guin SN, et al. Large anomalous Hall and Nernst effects in high Curie-temperature iron-based Heusler compounds. *Adv Sci*. 2021;8(17):2100782. doi: [10.1002/advs.202100782](https://doi.org/10.1002/advs.202100782)
- [54] Adachi H, Ando F, Hirai T, et al. Fundamentals and advances in transverse thermoelectrics. *Appl Phys Express*. 2025;18(9):090101. doi: [10.35848/1882-0786/adv700](https://doi.org/10.35848/1882-0786/adv700)

- [55] Zhou W, Sakuraba Y. Heat flux sensing by anomalous Nernst effect in Fe–Al thin films on a flexible substrate. *Appl Phys Express*. 2020;13(4):043001. doi: [10.35848/1882-0786/ab79fe](https://doi.org/10.35848/1882-0786/ab79fe)
- [56] Sakuraba Y. Potential of thermoelectric power generation using anomalous Nernst effect in magnetic materials. *Scr Mater*. 2016;111:29–32. doi: [10.1016/j.scriptamat.2015.04.034](https://doi.org/10.1016/j.scriptamat.2015.04.034)
- [57] Tanaka H, Higo T, Uesugi R, et al. Roll-to-roll printing of anomalous Nernst thermopile for direct sensing of perpendicular heat flux. *Adv Mater*. 2023;35(38):2303416. doi: [10.1002/adma.202303416](https://doi.org/10.1002/adma.202303416)
- [58] Yu H, Park SJ, Lee I, et al. Sign-reversed anomalous Nernst effect with matched Seebeck coefficient in lanthanide–iron alloys for the direct sensing of heat flux. *Sci Technol Adv Mater*. 2025;26(1):2544649. doi: [10.1080/14686996.2025.2544649](https://doi.org/10.1080/14686996.2025.2544649)
- [59] Abe R, Sekimoto Y, Saini S, et al. Round robin study on the thermal conductivity/diffusivity of a gold wire with a diameter of 30  $\mu\text{m}$  tested via five measurement methods. *J Therm Sci*. 2022;31(4):1037–1051. doi: [10.1007/s11630-022-1594-9](https://doi.org/10.1007/s11630-022-1594-9)
- [60] Zhou WX, Cheng Y, Chen KQ, et al. Thermal conductivity of amorphous materials. *Adv Funct Mater*. 2020;30(8):1903829. doi: [10.1002/adfm.201903829](https://doi.org/10.1002/adfm.201903829)
- [61] Miura A, Sepehri-Amin H, Masuda K, et al. Observation of anomalous Ettingshausen effect and large transverse thermoelectric conductivity in permanent magnets. *Appl Phys Lett*. 2019;115(22):222403. doi: [10.1063/1.5131001](https://doi.org/10.1063/1.5131001)
- [62] Miura A, Masuda K, Hirai T, et al. High-temperature dependence of anomalous Ettingshausen effect in  $\text{SmCo}_5$ -type permanent magnets. *Appl Phys Lett*. 2020;117(8):082408. doi: [10.1063/5.0023111](https://doi.org/10.1063/5.0023111)
- [63] Miura A, Iguchi R, Seki T, et al. Spin-mediated charge-to-heat current conversion phenomena in ferromagnetic binary alloys. *Phys Rev Mater*. 2020;4(3):034409. doi: [10.1103/PhysRevMaterials.4.034409](https://doi.org/10.1103/PhysRevMaterials.4.034409)
- [64] Watzman SJ, Duine RA, Tserkovnyak Y, et al. Magnon-drag thermopower and Nernst coefficient in Fe, Co, and Ni. *Phys Rev B*. 2016;94(14):144407. doi: [10.1103/PhysRevB.94.144407](https://doi.org/10.1103/PhysRevB.94.144407)
- [65] Yang Z, Codecido EA, Marquez J, et al. Scalable Nernst thermoelectric power using a coiled galfenol wire. *AIP Adv*. 2017;7(9):095017. doi: [10.1063/1.5003611](https://doi.org/10.1063/1.5003611)
- [66] Uchida K, Kuwabara T, Tanji T, et al. Anomalous Nernst thermoelectric generation in multilayer-laminated coiled magnetic wires. *Appl Phys Express*. 2023;16(9):093001. doi: [10.35848/1882-0786/acf645](https://doi.org/10.35848/1882-0786/acf645)